ISSN 2079-1704. Хімія, фізика та технологія поверхні. 2025. Т. 16. № 3. С. 322-338

UDC 621.315.5.001:53 doi: 10.15407/hftp16.03.322

S.I. Pokutnii [1, 2], T.Yu. Gromovoy [1], V.M. Ovdenko [2, 3]

ELECTRON STATES OF PEROVSKITES NANOCRYSTALS AND THE FUTURE OF SOLAR CELLS (MINI-REVIEW)

[1] Chuiko Institute of Surface Chemistry of National Academy of Sciences of Ukraine
17 Oleg Mudrak Str., Kyiv, 03164, Ukraine, E-mail: pokutnyi.serg@gmail.com, grota@ukr.net
[2] Institute of Physics of National Academy of Sciences of Ukraine
46 Nauky Ave., Kyiv, 03028, Ukraine
[3] Department of Macromolecular Chemistry, Taras Shevchenko National University of Kyiv
60 Volodymyrska Str., Kyiv, 01033, Ukraine, E-mail: valeryovdenko@gmail.com

Perovskite materials such as formamidinium lead bromide ($FAPbBr_3$) and ethylenediammonium-doped $FAPbBr_3$ ($\{en\}FAPbBr_3$) are widely utilized in nano-optoelectronic devices due to their relatively simple fabrication process, low cost, and high efficiency. Significant improvements have been achieved in theoretical and experimental studies of light emission and absorption, detection performance, and device design, especially for operation in the visible and near-infrared (NIR) regions. The possibilities of semiconductor perovskite solar cells (PSCs) as a reliable candidate for next-generation solar energy harvesting are considered.

It was shown theoretically that in a nanosystem interacting with low-intensity radiation, the oscillator strengths of transitions, as well as the dipole moments of transitions for single-particle electron quantum-confined states emerging in perovskites containing $FAPbBr_3$ and $\{en\}FAPbBr_3$ nanocrystals (NCs), took on values significantly (by two orders of magnitude) exceeding the typical values of the corresponding quantities for semiconductors. It has been found that at the resonant frequency of the electron transition, the values of the maximum optical absorption of NCs, as well as the NC polarizability, assume giant values (seven orders of magnitude) higher than the values of these quantities at other frequencies. This makes it possible to use such nanosystems as strongly absorbing nanomaterials in a wide range of infrared (IR) waves with a wavelength that can be varied across a wide range depending on the type of contacting materials.

Currently, new perovskite technologies are aiming to achieve the efficiency of crystalline silicon (Si). Compared to Si, PSCs have many advantages. Unlike Si, perovskites exhibit a direct bandgap, allowing for much more efficient absorption of light. As a result, only a thin film is required, reducing the cost of the manufacturing process (inexpensive solution processes). Unfortunately, a significant drawback is their sensitivity to moisture, air, and even light. Numerous research groups have experimented with various stabilization methods, but so far no PSC has demonstrated a durability close to that required for commercial solar cells (25 years). Instead of replacing Si, perovskite/Si tandem cells are expected to be the best solution. Because each material absorbs energy from different wavelengths of sunlight, perovskite/Si tandem cells have the potential to provide at least 20 % more energy efficiency than an Si cell. Tandem perovskite/Si photovoltaic cells have now achieved efficiencies of over 33 % in lab conditions, and their efficiency is much higher than that of Si and stand-alone cells.

***Keywords**: Perovskite nanocrystals (NCs), quantum dots (QDs), nano-optoelectronic devices, perovskite solar cells (PSCs), electron quantum-confined states*

INTRODUCTION

The mineral calcium titanate ($CaTiO_2$) was discovered by Gustav Rose in 1839 in the Urals and later named “perovskite” after the mineralogist L.A. Perovsky, who conducted extensive research into its structure. The term "perovskite" has come to refer to all compounds that have an identical or similar crystal structure to calcium titanate. Today, metal halide perovskites (MHPs**)** are promising nanomaterials for future applications, including typical optoelectronic nanodevices (photodetectors, light-emitting diodes (LEDs), lasers, solar cells), neuromorphic devices (“cutting-edge technologies”) such as artificial synapses/memristors, and finally pressure-induced devices [1–6]. The development of MHP research is driven by the progressive evolution of solid-state perovskite, which is considered a promising candidate for next-generation solar cells. The most efficient perovskite devices currently outperform standard multicrystalline (Si) solar cells, despite the fact that perovskites are typically grown at low temperatures using simple solution-based methods [7–14].

The widespread use of perovskites outside of photovoltaics (PV) is due to the ability to tune their optoelectronic properties in solar cells, photodetectors, and LEDs. These studies will influence the further technological development of nano-optoelectronic devices in the future [15–21].

Perovskites can be classified into three types based on dimensionality: 3D, 2D, and 0D perovskites, also known as quantum dots (QDs) (or nanocrystals (NCs)). Taking advantage of the obvious advantages of low-dimensional (0D, 1D, and 2D) perovskites, the integration of inorganic and organic materials at the molecular level makes it possible to create new structures of perovskite nanodevices. Hybrid low-dimensional (0D, 1D, and 2D)/3D device structures offer opportunities for enhanced thermal and optical stability, optimization of large-area device fabrication processes, exploration of internal physical mechanisms of devices, and innovative new functional devices [16–26]. Thus, the solvothermal synthesis of $CsPbBr_3$ NCs confirms their structural stability and optical prospects for photovoltaic applications [8].

In recent years, growing interest has been observed in the study of electron states with high binding energy and resistance to thermally-driven dissociation in perovskite nanostructured materials. These electron states are intensively used in devices for controlling electron and exciton transport processes, photon storage devices, transitions at the heterointerface of an exciton transistor, photoconversion, and photoluminescence (PL) in perovskite nanostructured materials [26–38]. In metal halide perovskite solar cells (PSCs), a significant increase in energy conversion efficiency was observed [30–38]. This is of particular interest, as perovskite hybrid chemical solar cells are emerging as promising candidates for wide commercial applications in PV [38, 39].

Perovskites containing colloidal NCs $FAPbBr_3$ and NCs $\{en\}FAPbBr_3$ are promising newcomers among optoelectronic materials. These nanomaterials have been used as highly absorbent nanolayers in solar cells. These new optoelectronic materials have attracted increased attention because of their high energy conversion efficiency, reaching about 20 % [39]. Perovskites, composed of colloidal NCs $FAPbBr_3$ and NCs $\{en\}FAPbBr_3$, belong to a new and developing class of semiconductors, in which, with the help of cation engineering, the bandgaps vary depending on the composition and size of NCs of the lead-halide [38, 40–44]. In [20], nanosystems consisting of colloidal NCs $FAPbBr_3$ and NCs $\{en\}FAPbBr_3$ were experimentally studied. It was found that doping bulk $FAPbBr_3$ perovskite with ethylenediammonium ({en}) led to an increase in the bandgap in NCs $\{en\}FAPbBr_3$. This caused an increase in the PL lifetimes in NCs $\{en\}FAPbBr_3$ compared to the PL lifetimes in NCs $FAPbBr_3$. In [20], PL lifetimes were also estimated in NCs $FAPbBr_3$ and NCs $\{en\}FAPbBr_3$. It was shown that the PL lifetimes in NCs $FAPbBr_3$ and NCs $\{en\}FAPbBr_3$ were formed by allowed electron transitions between the quantum-confined energy levels arising in NCs perovskites. The potential of such materials as active components in luminescent solar concentrators is highlighted in [45], which reviews light-emitting materials for enhancing solar energy capture. While organo-inorganic perovskites such as methylammonium lead iodide ($MAPbI_3$) and cesium lead halides ($CsPbX_3$, X = Br, I) have dominated research due to their high efficiencies (up to 25.7 % for single-junction devices [38]) and ease of synthesis, with thousands of publications detailing their optoelectronic properties, stability challenges, and scalability, $FAPbBr_3$ and $\{en\}FAPbBr_3$ NCs remain less explored, particularly regarding their intraband optical absorption. This mini-review focuses on these specific NCs because of their distinctive advantages: superior near-infrared (NIR) absorption compared to iodide-based counterparts, enhanced structural and thermal stability through formamidinium (FA) cation incorporation, and the ability to tune optical properties via ethylenediammonium ({en}) doping, unlike $MAPbXI_3$, which suffers from moisture sensitivity and phase instability under ambient conditions [31]. The addition of {en} in $\{en\}FAPbBr_3$ further stabilizes the perovskite lattice, widens the bandgap, and extends carrier lifetimes, making it a compelling candidate for tandem solar cells and nanophotonic applications [19, 30]. This gap in understanding, amidst the extensive literature on organo-inorganic perovskites, motivates their selection to unlock new pathways for exceeding current PV efficiency limits and advancing NIR-responsive technologies [19, 34, 36–40]. Therefore, in the present work, within the framework of the dipole approximation, the intraband optical absorption due to allowed transitions between one-particle

electron quantum-confined states emerging in the NCs $FAPbBr_3$ is investigated. Studies on solvothermal synthesis of $CsPbBr_3$ NCs confirm their structural stability and optical promise for PV applications [8], while dopant concentration effects in perovskite QDs highlight their tunability [6]. Photochemical processes involving graphene oxide, which could enhance charge transfer in such systems, are discussed in [46], providing insights into hybrid nanomaterial interactions.

Application of these NCs can increase the efficiency of PSCs, which without any additives already achieve an efficiency beyond 25 %, and up to 34 % in tandem configurations [38]. By appropriate tailoring of nano-admixtures, it is, however, possible to surpass the Shockley–Queisser efficiency limit in these cells. Using metallic nano-components, an even 40 % relative increase in the efficiency of a perovskite cell has been experimentally demonstrated [39]. This is even larger than that in conventional (Si or copper indium gallium selenide (CIGS)) cells [47] and reflects the fact that in chemical cells without *p-n* junction, a different plasmonic photovoltaic effect dominates [48, 49]. Simultaneous application of additional NCs would result in further increase in efficiency and in a completely yet unexplored synergetic effect of NC-metallic nanoparticle complexes. Coupling of excitons in NCs with surface plasmons in metallic nanoparticles, sensitive to the proximity of both subsystems, would beneficially influence both nano-agents in a different way than separately. This additionally motivates the presented study.

Electron and exciton states with high binding energy and resistance to thermally-driven dissociation play an important role in many prospective perovskite nanostructured materials. In recent years, growing interest in the electron and exciton states adjustment for controlling exciton transport processes, transitions at the heterointerface of the excitonic transistor, photoconversion, nanostructure PL, and optical properties of dielectric and semiconductor nanostructures [20, 21]. These devices include traps, lattices, conveyors, and ramps, which are used for studying basic properties of cold electron states, as well as electron transistors, routers, and photon storage devices, which hold the potential for creating exciton signal processing devices and exciton and electron circuits [20–25]. Investigations into dopant concentration effects in perovskite QDs further emphasize their tunable optical properties for such applications [6].

Perovskites containing colloidal QDs $FAPbBr_3$ are promising newcomer optoelectronic materials. These nanomaterials have been used as highly absorbent nanolayers in solar cells. These newcomer optoelectronic materials have attracted increased attention because of their high solar energy conversion efficiency, reaching about 20 % [25].

For intensive application of nanomaterials containing perovskite NCs (or QDs), it is necessary to find nanomaterials that strongly absorb light in the visible and IR ranges. In [21], the theory of electron quantum-confined states in colloidal QDs $FAPbBr_3$ was developed. These nanomaterials have been shown to be highly absorbing nanomaterials over a wide range of visible and IR wavelengths with wavelengths that can be varied across a wide range depending on the type of contacting materials. These nanomaterials containing perovskite NCs (or QDs) can be used as active elements that efficiently convert solar energy into electrical energy in solar cells. The use of semiconductor nanoparticles in photoelectrochemical solar cells with liquid electrolytes, potentially applicable to perovskite systems, is reviewed in [50], emphasizing their photovoltaic potential.

The mini-review analyzes the potential of using perovskite NCs in solar cells. This emphasis on $FAPbBr_3$ and $\{en\}FAPbBr_3$ NCs leverages their unique NIR absorption, stability enhancements via cation doping, and underexplored intraband transitions to address gaps in the extensive literature on organo-inorganic perovskites, offering insights into next-generation PV solutions beyond widely studied $MAPbI_3$ and $CsPbX_3$ [19]. It is shown that perovskites containing colloidal QDs $FAPbBr_3$ nanosystems are highly absorbing media in the IR region in weak optical fields. In these nanosystems, the polarizability, absorption cross-section, radiation intensity, and also the optical attenuation coefficient of light take on gigantic values, which are two orders of magnitude higher than the corresponding values in semiconductors. The obtained results can be used for creating nano- and heterostructures for advanced nanophotonic applications that operate under conditions of weak optical fields in the IR region.

OPTICAL TRANSITIONS BETWEEN ELECTRON QUANTUM-CONFINED STATES IN PEROVSKITE NANOCRYSTALS

In the experimental work [20], NCs of perovskites $FAPbBr_3$ and {en}$FAPbBr_3$ were studied. It was assumed that the NCs were spherical with average radii $a = 5.5$ nm. The values of broadenings of the absorption edge $\Delta E_1 = 71$ meV for NC $FAPbBr_3$, and $\Delta E_2 = 120$ meV for NC {en}$FAPbBr_3$ were determined. The studied NC perovskites had the following optical characteristics: dielectric constant ε; m_e and m_h are effective electron and hole masses, respectively; exciton reduced mass is calculated as $\mu_{ex} = (m_e m_h)/(m_e + m_h)$; the Bohr radii are $a_e = (\varepsilon\hbar^2/m_e e^2)$ for an electron; $a_h = (\varepsilon\hbar^2/m_h e^2)$ for a hole; and $a_{ex} = (\varepsilon\hbar^2/\mu_{ex} e^2)$ for an exciton. In QDs perovskite $FAPbBr_3$, such optical characteristics took the following values: $\varepsilon = 8.6$, $m_e = 0.26\, m_0$ and $m_h = 0.26\, m_0$, $\mu_{ex} = 0.13\, m_0$ (m_0 is the mass of a free electron), $a_e = 1.75$ nm, $a_h = 1.75$ nm, $a_{ex} = 3.5$ nm. In NCs perovskite {en}$FAPbBr_3$, such optical characteristics took the following values: $\varepsilon = 7$, $m_e = 0.21\, m_0$ and $m_h = 0.21\, m_0$, $\mu_{ex} = 0.105\, m_0$, $a_e = 1.8$ nm, $a_h = 1.8$ nm, $a_{ex} = 3.6$ nm.

In [21], the NC was modeled by a spherical potential well with infinitely deep walls. In this case, the energy levels of an electron (n_e, l_e) and a hole (n_h, l_h) were determined by the formula [22]:

$$E_{n,l}^{e(h)}(a) = \frac{\hbar^2}{2m_{e(h)}\, a^2}\,(X_{n,l})^2, \qquad (1)$$

where the subscripts (n, l) are the principal and azimuthal quantum numbers for the electron (hole); and $X_{n,l}$ are the roots of the Bessel function, i.e., $J_{l+1/2}(X_{n,l}) = 0$. Energy levels of an electron $E_{n,l}^{(e)}(a)$ (1) and a hole $E_{n,l}^{(h)}(a)$ (1) were in the conduction and valence bands NC. Assume that the quantum-confined levels of the electron energy $E_{n,l}^{e}(a)$ (1) the NC are slightly broadened at temperature T, i.e. the energy separation between the levels is

$$\Delta E_{n,l}^{e}(a) = E_{n,l+1}^{e}(a) - E_{n,l}^{e}(a) \ll kT. \qquad (2)$$

When condition (2) is satisfied, the electron states (1) in the NC can be observed. These electron states (1) can be described by the wave functions of an electron in a spherical quantum well with infinitely high walls [20, 21].

In [20], it was shown that the broadening $\Delta E_1 = 71$ meV of the absorption edge in the NC $FAPbBr_3$ was caused by two allowable transitions between the quantum-confined states of an electron $(n_e = 1, l_e = 0, t_e = 0)$ and $(n_e = 1, l_e = 1, t_e = 1)$, as well as $(n_e = 1, l_e = 1, t_e = 1)$ and $(n_e = 1, l_e = 2, t_e = 0)$ (where t is the magnetic quantum number of the electron). The transition energies, according to formula (1), between these electron levels were $\Delta E_{1,0,0}^{1,1,1}(a) = 51.2$ meV and $\Delta E_{1,1,1}^{1,2,0}(a) = 65.4$ meV. The broadening value of $\Delta E_1 = 71$ meV of the absorption edge in NCs $FAPbBr_3$ with an accuracy not exceeding 14 % was caused by these transitions [20]. Doping led to a change in the optical characteristics of {en}$FAPbBr_3$ NC compared to the optical characteristics of $FAPbBr_3$ NC [20]. In this case, the broadening of the $\Delta E_2 = 120$ meV absorption edge in the {en}$FAPbBr_3$ NC was caused by three allowable transitions between quantum size – confined states of an electron $(n_e = 1, l_e = 0, t_e = 0)$ and $(n_e = 1, l_e = 1, t_e = 1)$, $(n_e = 1, l_e = 1, t_e = 1)$ and $(n_e = 1, l_e = 2, t_e = 0)$, as well as $(n_e = 1, l_e = 2, t_e = 0)$ and $(n_e = 1, l_e = 3, t_e = 1)$, with transition energies $\Delta E_{1,0,0}^{1,1,1}(a) = 64$ meV, $\Delta E_{1,1,1}^{1,2,0}(a) = 82$ meV and $\Delta E_{1,2,0}^{1,3,1}(a) = 112$ meV respectively. The broadening value of $\Delta E_2 = 120$ meV of the absorption edge in NCs $\{en\}FAPbBr_3$, with an accuracy not exceeding 10% was caused by these transitions [20].

Quantum-confined states of electron (n_e, l_e) (1) in NCs in the field of a light wave was adequately described in the dipole approximation [22]. Let us write an expression for the dipole moments of the allowable transitions $D_{n,l,t}^{n,l+1,t}(a)$ between the quantum-confined states of an electron $(n_e = 1, l_e, t)$ and $(n_e = 1, l_e + 1, t)$ in NCs (where the azimuthal quantum number of the electron $l_e \le 2$, and the magnetic quantum number of electron $t = 0.1$) [24, 25]:

$$D_{1,l,t}^{1,l+1,t}(a) = \left\langle \Psi_{1,l+1,t}(r,\theta) \middle| D(r) \middle| \Psi_{1,l,t}(r,\theta) \right\rangle, \qquad (3)$$

where the operator of the dipole moment of the electron located in the NC is expressed as [21]

$$D(r) = \Lambda e r. \qquad (4)$$

In formula (4), the nanosystem parameter

$$\Lambda = 3\varepsilon_0/(2\varepsilon_0 + \varepsilon), \quad (5)$$

(here ε_0 is the permittivity matrix and $\varepsilon_0 = 1$), r is the radius vector determining the distance between the electron and the center of the NC, θ is the azimuthal angle defining the position of electron radius vector. In formula (3), the states $|n_e = 1, l_e, t\rangle$ and $|n_e = 1, l_e + 1, t\rangle$ electron are described by electron wave functions $\Psi_{1,l,t}(r,\theta)$ and $\Psi_{1,l+1,t}(r,\theta)$ of an infinitely deep spherical potential well.

Using formulas (3) – (5), expressions were obtained that describe the values of the dipole moments $D_{n,l,t}^{n,l+1,t}(a)$ of admissible transitions between the quantum-confined states of an electron $(n_e = 1, l_e, t)$ and $(n_e = 1, l_e + 1, t)$ (where $l_e \le 2, t = 0, 1$) in NCs [21]. Oscillator strengths of the allowable transitions $f_{n,l,t}^{n,l+1,t}(a)$ between the quantum-confined states of an electron $(n_e = 1, l_e, t)$ and $(n_e = 1, l_e + 1, t)$ were presented in [21]:

$$f_{1,l,t}^{1,l+1,t}(a) = (X_{1,l+1}{}^2 - X_{1,l}{}^2)\left|\frac{D_{1,l,t}^{1,l+1,t}(a)}{ea}\right|^2. \quad (6)$$

Here $X_{n,l}$ are the roots of the Bessel function, i.e., $J_{l+1/2}(X_{n,l}) = 0$.

Intensity $I_{1,l,t}^{1,l+1,t}(a)$, caused by dipole-allowed intraband electron transitions between the quantum-confined states $(n = 1, l, t)$ and $(n = 1, l + 1, t)$, was determined by the square of the overlap integral of the electron wave functions $\Psi_{1,l,t}(r,\theta)$ and $\Psi_{1,l+1,t}(r,\theta)$ [22]

$$I_{1,l,t}^{1,l+1,t}(a) = C\left|\int_0^{2\pi} d\varphi \int_0^{\pi} d\theta sin\theta \int_0^{a} drr^2\, \Psi_{1,l+1,t}(r,\theta,\varphi)\, \Psi_{1,l,t}(r,\theta,\varphi)\right|^2 \delta\left(\hbar\omega - \hbar\omega_{1,l+1;1,l}(a)\right). \quad (7)$$

In (7), C is the quantity proportional to the square of the modulus of the matrix element of the dipole moment, taken for the Bloch functions of the conduction band of NC, ω is the frequency of the emitting light, the radiation energy $\hbar\omega_{1,l+1;1,l}(a) = E_{1,l+1}(a) - E_{1,l}(a)$. After integration in (7), taking into account (6)–(9), expressions were obtained describing the intensities $I_{1,l,t}^{1,l+1,t}(a)$ of the dipole-allowed electron transitions between the quantum-confined states $(n = 1, l, t)$ and $(n = 1, l + 1, t)$ (where $l \le 2, t = 0, 1$) in NCs [21].

OPTICAL ABSORPTION ON QUANTUM-CONFINED ELECTRON STATES IN A NANOSYSTEM

The cross section of light absorption $\sigma_{abs}(\omega, a)$ on the spherical surface of a NC of radius α can be expressed in terms of its polarizability $A''(\omega, a)$ [21]:

$$\sigma_{abs}(\omega,a) = 4\pi\,(\omega/c)\,|A''(\omega, a)|, \quad (8)$$

ω is the frequency of absorbed light and c is the speed of light in vacuum. When condition (2) was satisfied, as well as for slightly broadened electron states (1), for which the widths $\Gamma_{n,l}(a)$ of the quantum-confined levels (n, l) (1) are small compared to frequencies $\omega_{n,l}(a)$, i.e. at

$$\Gamma_{n,l}(a) << \omega_{n,l}(a), \quad (9)$$

NC can be represented as a single superatom [20] (where $\omega_{1,l}(a) = E_{1,l}(a)/\hbar$ is the frequency corresponding to the electron quantum-confined energy level $E_{1,l}(a)$ (1)). In this case, the polarizability $A''(\omega, a)$ of NC was described by the formula [21]:

$$A''(\omega, a) = \frac{e^2}{m_e}\sum_{n,l} f_{n,l,t}^{n,l+1,t}\left[\frac{\omega_{n,l+1}^2(a) - \omega^2}{(\omega_{n,l+1}^2(a) - \omega^2)^2 + (\omega\Gamma_{n,l+1})^2} + i\frac{\omega\Gamma_{n,l+1}}{(\omega_{n,l+1}^2(a) - \omega^2)^2 + (\omega\Gamma_{n,l+1})^2}\right]. \quad (10)$$

In (10) oscillator strengths of the allowable transitions $f_{n,l,t}^{n,l+1,t}(a)$ between the quantum-confined states of an electron $(n_e = 1, l_e, t)$ and $(n_e = 1, l_e + 1, t)$ are defined by formula (6).

Let us consider the behavior of NCs in weak optical fields. Let us assume that in these fields the polarizability $A''(\omega, a)$ (9) of the NC was caused to only one electron transition between the quantum-confined states $(n_e = 1, l_e, t)$ and $(n_e = 1, l_e + 1, t)$. In this case, the polarizability (10) of the NC is determined by the expression [21]:

$$A''(\omega, a) = f_{n,l}^{n,l+1}(a)\frac{e^2}{m_e}\left[\frac{\omega_{n,l+1}^2(a) - \omega^2}{(\omega_{n,l+1}^2(a) - \omega^2)^2 + (\omega\Gamma_{n,l+1})^2} + i\frac{\omega\Gamma_{n,l+1}}{(\omega_{n,l+1}^2(a) - \omega^2)^2 + (\omega\Gamma_{n,l+1})^2}\right]. \quad (11)$$

Consider the case in which the frequency of light ω is significantly lower and far from the resonant electron state (n, l+1) frequency $\omega_{n,l+1}(a)$ (i. e. $\omega^2 \ll \left(\omega_{n,l+1}(a)\right)^2$. Taking into account (1), we write the polarizability (10) as [21]

$$A_1''(a) \approx 4(m_e\ /m_{\rm o}\ )\ ({X_{1,l+1}}^2 - {X_{1,l}}^2)\ (X_{n,l+1})^{-4}\ \left|D_{1,l,t}^{1,l+1,t}(a)/ea\right|^2\ (a/a_{\rm o}\ )^4\ (a_{\rm o})^3, \quad (12)$$

where $a_{\rm o} = 0.053$ nm is the Bohr radius of a free electron. We neglect the real part of the polarizability (11) NC for frequencies close to resonant $\omega \approx \omega_{n,l+1}(a)$, since it is much smaller than the imaginary part. As a result, we obtain an expression that describes the polarizability of NC [21]:

$$A_2''(a) \approx i\ 4\ ({X_{1,l+1}}^2 - {X_{1,l}}^2)(X_{n,l+1})^{-2}\ (Ry_{\rm o}\ /\hbar\Gamma_{n,l+1})\left|D_{1,l,t}^{1,l+1,t}(a)/ea\right|^2 (a/a_{\rm o}\ )^2\ (a_{\rm o})^3, \quad (13)$$

where $Ry_{\rm o}$ =13.606 eV is the Rydberg constant. In the case $\omega \gg \omega_{1,l+1}$ (i. e. $\omega^2 \gg (\omega_{n,l+1}(a))^2$ the polarizability of NC is given by a negative real part [21, 22]:

$$A_3''(a) \approx -\ 4(Ry_{\rm o}\ /E_\omega)^2\ ({X_{1,l+1}}^2 - {X_{1,l}}^2)\left|D_{1,l,t}^{1,l+1,t}(a)/ea\right|^2 (m_0\ /m_e\ )\ (a_{\rm o})^3, \quad (14)$$

where $E_\omega = \hbar\omega$.

The behavior we have considered of the quantum-confined states of an electron arising in NC, in the field of a light wave are applicable to an ensemble of non-interacting NC, i.e., to the NC ensemble with the NC concentration N [51]:

$$a\ N^{\frac{1}{3}} \ll 1. \quad (15)$$

Let us carry out numerical estimates of dipole moments of allowable intraband transitions $D_{1,l,t}^{1,l+1,t}$ (3), oscillator strengths of allowable intraband transitions $f_{1,l,t}^{1,l+1,t}$ (6), and intensities $I_{1,l,t}^{1,l+1,t}$ (7) of dipole-allowed intraband electron transitions between the quantum-confined states $(n = 1, l, t)$ and $(n = 1, l + 1, t)$ (where $l \leq 2, t = 0, 1)$ in spherical NCs with radius a = 5.5 nm, containing perovskites $\rm FAPbBr_3$ (for $l = 0{,}1$) (see Table 1) and $\rm \{en\}FAPbBr_3$ (for $l = 0{,}1{,}2$) (see Table 2). From formulas (3)–(5) and (8)–(10) it follows that the values of dipole moments of allowable transitions $D_{1,l,t}^{1,l+1,t}$ (3), oscillator strengths of allowable transitions $f_{1,l,t}^{1,l+1,t}$ (6), as well as the intensities $I_{1,l,t}^{1,l+1,t}$ (7) of dipole-allowed electron transitions with increasing azimuthal quantum number l (from 0 to 1) for perovskites $\rm FAPbBr_3$, and l (from 0 to 2) for perovskites $\rm \{en\}FAPbBr_3$) decrease in proportion to the coefficient $({X_{1,l+1}}^2 - {X_{1,l}}^2)^{-1}$ (where $X_{1,0} = \pi$; $X_{1,1} = 4.493$; $X_{1,2} = 5.763$; $X_{1,3} = 6.988$ are the roots of the Bessel function i.e., $J_{l+1/2}\ (X_{n,l}) = 0$ [24]). In this case, the values of dipole moments $D_{1,l,t}^{1,l+1,t}$ (3) in NC perovskites $\rm \{en\}FAPbBr_3$ (for $l \leq 2$) will exceed the corresponding values of dipole moments in NC perovskites $\rm FAPbBr_3$ (for $l = 0{,}1$) (see Tables 1 and 2). This is due to the fact that according to formulas (4) and (5) of dipole moments (3) are proportional to the coefficient Λ (5). The coefficient Λ (5) is inversely proportional to the permittivity ε NCs. Since in NC perovskites $\rm FAPbBr_3$ the permittivity ε = 8.6 is greater than the value ε = 7 in NC perovskites $\rm \{en\}FAPbBr_3$, then the coefficient $\Lambda = 3^{-1}$ for NC perovskites $\rm \{en\}FAPbBr_3$ will exceed $\Lambda = 0.28$ in NC perovskites $\rm FAPbBr_3$.

Table 1. The estimated values of oscillator strength $f_{1,l,t}^{1,l+1,t}$ (6), transition dipole moments $D_{1,l,t}^{1,l+1,t}$ (3) (where $D_0 = e$Å in Debye units) and radiation intensity $I_{1,l,t}^{1,l+1,t}$ (7) caused by dipole-allowed electron transitions between the quantum-confined states $(n = 1, l, t) \rightarrow (n = 1, l + 1, t)$ (where $l =$ 0, 1 and $t =$ 0, 1) in NC perovskites $\rm FAPbBr_3$ with radius a = 5.5 nm

$(1, l, t) \rightarrow (1, l{+}1, t)$	$f_{1,l,t}^{1,l+1,t}$	$D_{1,l,t}^{1,l+1,t}\ (D_0)$	$I_{1,l,t}^{1,l+1,t}$
(1,0,0) → (1,1,1)	0.24	8.4	0.65
(1,l,1) → (1,2,0)	0.14	5.7	0.31

Table 2. The estimated values of oscillator strength $f_{1,l,t}^{1,l+1,t}$ (6) transition dipole moments $D_{1,l,t}^{1,l+1,t}$ (3) (where $D_0 = e$Å in Debye units) and radiation intensity $I_{1,l,t}^{1,l+1,t}$ (7) caused by dipole-allowed electron transitions between the quantum-confined states $(n = 1, l, t) \rightarrow (n = 1, l + 1, t)$ (where $l =$ 0, 1, 2 and $t =$ 0, 1) in NC perovskites {en}$FAPbBr_3$ with radius α = 5.5 nm

$(1, l, t) \rightarrow (1, l+1, t)$	$f_{1,l,t}^{1,l+1,t}$	$D_{1,l,t}^{1,l+1,t}$ (D_0)	$I_{1,l,t}^{1,l+1,t}$
(1,0,0) → (1,1,1)	0.33	9.9	0.65
(1,l,1) → (1,2,0)	0.194	6.72	0.31
(1,2,0) → (1,3,1)	0.045	2.96	0.20

The values of dipole moments $D_{1,l,t}^{1,l+1,t}$, according to formulas (10)–(13), as well as of oscillator strengths of allowable transitions $f_{1,l,t}^{1,l+1,t}$ (6) with increasing azimuthal quantum number l (from 0 to 1) decrease from $D_{1,0,0}^{1,1,1} = 8.4\,D_0$ to $D_{1,1,1}^{1,2,0} = 5.7\ D_0$ (where $D_0 = e$Å in Debye units) and from $f_{1,0,0}^{1,1,1} = 0.24$ to $f_{1,1,1}^{1,2,0} = 0.14$ in NC perovskites $FAPbBr_3$ (see Table 1), and also decrease from $D_{1,0,0}^{1,1,1} = 9.9$ to $D_{1,2,0}^{1,3,1} = 2.96$ and from $f_{1,0,0}^{1,1,1} = 0.33$ to $f_{1,2,0}^{1,3,1} = 0.045$ in NC perovskites {en}$FAPbBr_3$ with increasing l (from 0 to 2) (see Table 2). As azimuthal quantum number l increases (from 0 to 2), the intensities $I_{1,l,t}^{1,l+1,t}$ (17) of the dipole-allowed electron transitions in NC perovskites {en}$FAPbBr_3$ also decrease from $I_{1,0,0}^{1,1,1} = 0.65$ to $I_{1,2,0}^{1,3,1} = 0.20$ (see Table 2). The intensity values (16) in in NC perovskites $FAPbBr_3$ decrease from $I_{1,0,0}^{1,1,1} = 0.65$ to $I_{1,1,1}^{1,2,0} = 0.31$ as l decreases from 0 to 1 (see Table 1).

Tables 3 and 4 show the numerical values of polarizabilities $A_1''(a)$ (12) (in case, when the frequency of light ω is significantly lower and far from the resonant electron state $(n,\ l+1)$ frequency $\omega_{n,l+1}(a)$, at $\left(\omega/\omega_{1,l+1}\right)^2 = 10^{-2}$), as well as the absorption cross sections $\sigma_{abs}(\omega, a)$ (10), which were due to dipole-allowed electron transitions between the quantum-confined states $(n = 1, l, t)$ and $(n = 1, l + 1, t)$ (where $l \leq 2$, $t = 0, 1$) in spherical NCs with radius a = 5.5 nm, containing perovskites $FAPbBr_3$ (for $l =$ 0, 1) and {en}$FAPbBr_3$ (for $l \leq 2$). Polarizabilities A_1'' (12), as well as the corresponding absorption cross sections $\sigma_{abs}(\omega,a)$ (10), according to formulas (10)–(14), with increasing azimuthal quantum number l (from 0 to 1) for perovskites $FAPbBr_3$, and l (from 0 to 2) for perovskites {en}$FAPbBr_3$ decrease in proportion to the coefficient $(X_{1,l+1}{}^2 - X_{1,l}{}^2)^{-1}(X_{n,l+1})^{-4}$. The values of polarizabilities A_1'' (12) and absorption cross sections $\sigma_{abs}(\omega, a)$ (10) with increasing l (from 0 to 1) decrease from $A_1'' = 1.1 \cdot 10^{-20}\text{cm}^3$ (and $\sigma_{abs} = 6.5 \cdot 10^{-17}\text{cm}^2$) to $A_1'' = 5.4 \cdot 10^{-21}\text{cm}^3$ (and $\sigma_{abs} = 5.5 \cdot 10^{-17}\text{cm}^2$ in NC perovskites $FAPbBr_3$ (see Table 3), and also decrease from $A_1'' = 8.56 \cdot 10^{-21}\text{cm}^3$ (and $\sigma_{abs} = 6.7 \cdot 10^{-17}\text{cm}^2$) to $A_1'' = 2.8 \cdot 10^{-22}\text{cm}^3$ (and $\sigma_{abs} = 4.35 \cdot 10^{-18}\text{cm}^2$) in NC perovskites {en}$FAPbBr_3$ with increasing l (from 0 to 2) (see Table 4). Since the polarizabilities (12) and absorption cross sections (10) are proportional to the ratio $(m_e\ /m_0\ )$, and the effective mass of the electron in NC perovskites $FAPbBr_3$ is greater than the effective mass of the electron in NC perovskites {en}$FAPbBr_3$, then the values of polarizabilities A_1'' (12) and absorption cross sections $\sigma_{abs}(\omega, a)$ (10) in in NC perovskites $FAPbBr_3$ exceed the corresponding values of polarizabilities (12) and absorption cross sections (10) in NC perovskites {en}$FAPbBr_3$ (see Tables 3 and 4). The frequencies $\omega_{1,l}(a)$ are in the infrared region.

Tables 3 and 4 show the numerical values of polarizabilities $A_2''(a)$ (13) and absorption cross sections $\sigma_{abs}(\omega,\ a)$ (10) in NC perovskites $FAPbBr_3$, as well as the values of polarizabilities (14) and absorption cross sections (10) in NC perovskites {en}$FAPbBr_3$ at resonant absorption of light with frequencies $\omega \approx \omega_{1,l+1}(a)$. These values, according to formulas (11)–(14), (for the ratio $((\hbar\Gamma_{1,l+1}/E_{1,l+1}) = 10^{-2})$, are three orders of magnitude higher than the corresponding values of polarizabilities (13) and absorption cross sections (10) in case $\left(\left(\omega/\omega_{1,l+1}\right)^2 = 10^{-2}\right)$.

According to formula (7), the values of polarizabilities $A_3''(a)$ (14) and absorption cross sections $\sigma_{abs}(\omega,\ a)$ (10) in NC perovskites $FAPbBr_3$ and NC perovskites {en}$FAPbBr_3$ for

frequencies ω (for $\left(\omega/\omega_{1,l+1}\right)^2 = 10^2$), will be two orders of magnitude smaller than the corresponding values of polarizabilities (13) and absorption cross sections (10) in the case ($\left(\omega/\omega_{1,l+1}\right)^2 = 10^{-2}$) (see Tables 3 and 4).

Table 3. The estimated values of of polarizabilities $A_1''(a)$ (12) (for $\left(\omega/\omega_{1,l+1}\right)^2 = 10^{-2}$)), $A_2''(a)$ (13) (for $\approx \omega_{1,l+1}(a)$), $A_3''(a)$ (14) (for $\left(\omega/\omega_{1,l+1}\right)^2 = 10^{-2}$) (where ω is the frequency of the absorbed light and the resonant electron state (n, l+1) frequency $\omega_{n,l+1}(a)$), as well as the corresponding absorption cross sections $\sigma_{abs}(\omega, a)$ (10) caused by dipole-allowed electron transitions between the quantum-confined states $(n = 1, l, t) \rightarrow (n = 1, l + 1, t)$ (where $l =$ 0, 1 and $t =$ 0, 1) in NC perovskites $FAPbBr_3$ with radius α = 5.5 nm

$(1, l, t) \rightarrow (1, l+1, t)$	$\left(\omega/\omega_{1,l+1}\right)^2$	$\lvert A''(\omega, a)\rvert$ $(10^{-22}\mathrm{cm}^3)$	σ_{abs} $(10^{-22}\mathrm{cm}^2)$
(1,0,0) → (1, 1,1)	10^{-2}	$1.1 \cdot 10^2$	$6.5 \cdot 10^5$
(1,0,0) → (1, 1,1)	1	$1.1 \cdot 10^4$	$7.1 \cdot 10^8$
(1,0,0) → (1, 1,1)	10^2	1	$6.3 \cdot 10^5$
(1,1,1) → (1,2,0)	10^{-2}	$5.4 \cdot 10^1$	$5.5 \cdot 10^5$
(1,1,1) → (1,2,0)	1	$3.9 \cdot 10^3$	$4 \cdot 10^8$
(1,1,1) → (1,2,0)	10^2	$6 \cdot 10^{-1}$	$6 \cdot 10^5$

Table 4. The estimated values of of polarizabilities $A_1''(a)$ (12) (for $\left(\omega/\omega_{1,l+1}\right)^2 = 10^{-2}$)), $A_2''(a)$ (13) (for $\approx \omega_{1,l+1}(a)$), $A_3''(a)$ (14) (for $\left(\omega/\omega_{1,l+1}\right)^2 = 10^{-2}$) (where ω is the frequency of the absorbed light and the resonant electron state (n, l+1) frequency $\omega_{n,l+1}(a)$), as well as the corresponding absorption cross sections $\sigma_{abs}(\omega, a)$ (10) caused by dipole-allowed electron transitions between the quantum-confined states $(n = 1, l, t) \rightarrow (n = 1, l + 1, t)$ (where $l =$ 0, 1, 2 and $t =$ 0, 1) in NC perovskites {en}$FAPbBr_3$ with radius α = 5.5 nm

$(1, l, t) \rightarrow (1, l+1, t)$	$\left(\omega/\omega_{1,l+1}\right)^2$	$\lvert A''(\omega, a)\rvert$ $(10^{-22}\mathrm{cm}^3)$	σ_{abs} $(10^{-22}\mathrm{cm}^2)$
(1,0,0) → (1, 1,1)	10^{-2}	$8.56 \cdot 10^1$	$6.7 \cdot 10^5$
(1,0,0) → (1, 1,1)	1	$9 \cdot 10^3$	$7 \cdot 10^8$
(1,0,0) → (1, 1,1)	10^2	$8.4 \cdot 10^{-1}$	$6.5 \cdot 10^5$
(1,1,1) → (1,2,0)	10^{-2}	$4.4 \cdot 10^1$	$5.5 \cdot 10^5$
(1,1,1) → (1,2,0)	1	$3.2 \cdot 10^3$	$4 \cdot 10^8$
(1,1,1) → (1,2,0)	10^2	$2.6 \cdot 10^{-1}$	$3.2 \cdot 10^5$
(1,2,0) → (1,3,1)	10^{-2}	2.8	$4.35 \cdot 10^4$
(1,2,0) → (1,3,1)	1	$2.6 \cdot 10^2$	$1.5 \cdot 10^8$
(1,2,0) → (1,3,1)	10^2	$2.8 \cdot 10^{-2}$	$5.1 \cdot 10^4$

The optical attenuation coefficient $\gamma(\omega, a)$ of light, due to both absorption and scattering of light by quantum-confined states electron (n, l) (1) in NCs perovskite $FAPbBr_3$ and NCs perovskite {en}$FAPbBr_3$, of radius a is determined by the expression [51–53]

$$\gamma(\omega, a) = N\,(\sigma_{abs}(\omega,a) + \sigma_{sc}(\omega,a)), \qquad (16)$$

where N is the concentration of NCs perovskite $FAPbBr_3$ and NCs perovskite $\{en\}FAPbBr_3$ in the nanosystem. Formula (16) was obtained for an ensemble of non-interacting NCs. In this case, condition (15) is satisfied.

In formula (16) included the cross section for scattering $\sigma_{sc}(\omega, a)$ of light by a NC. Now we write the expression for the cross section $\sigma_{sc}(\omega, a)$ of elastic scattering of the electromagnetic wave with frequency ω by the NC of radius a [51] as:

$$\sigma_{sc}\,(\omega, a) = 2^7\, 3^{-3}\, \pi^3\, (\omega/c)^4\, |A''(\omega, a)|^{\,2}. \qquad (17)$$

Formula (17) includes the cross section for scattering $\sigma_{sc}\,(\omega,a)$ of light by a NC. Since,

according to (17) $\sigma_{sc}(\omega,a) \sim |A''(\omega,a)|^2$, then the values of the scattering cross section $\sigma_{sc}(\omega,a)$ (17) are six orders of magnitude smaller than the corresponding values $\sigma_{abs}(\omega,a)$ (10). Therefore, to estimate the optical attenuation coefficient $\gamma(\omega, a)$ (16), the processes of light scattering are not taken into account.

Thus, nanosystems containing NCs perovskite $FAPbBr_3$ and NCs perovskite $\{en\}FAPbBr_3$ are highly absorbing media in the infrared range. In nanosystems containing NCs perovskite $FAPbBr_3$ and NCs perovskite $\{en\}FAPbBr_3$ with a concentration of NCs $N \approx (10^{14} - 10^{16})\ \mathrm{cm}^{-3}$ [20] the optical attenuation coefficient (16) coefficient takes on a significant value $\gamma(\omega, a) \approx (1 - 10^2)\ \mathrm{cm}^{-1}$. Nanostructured perovskite materials can further enhance absorption, offering avenues for next-generation PV technologies [4].

The increase of the absorption due NCs application is of high significance in perovskite solar cells. As was proved [20], the strengthening of the sun-light absorption by using of nano-components leads to increase of the overall efficiency of solar cells. In *p-n* junction cells quantum coupling of nano-localized plasmons to band electrons can even double the photo-efficiency just by the increase of the absorption [20]. In perovskite cells this channel is, however, ineffective [21, 22] and localized plasmons contribute rather to internal electrical phenomena in cells. Application of NCs simultaneously with metallic nanoparticles would activate both channels simultaneously – absorption and electrical one.

In [53] the absorption and photoluminescence of light from NC perovskite $CsPbBr_3$ was experimentally studied. A peak was obtained in the absorption spectrum at 498 nm (2.493 eV). A photoluminescence peak was also observed at 508 nm (2.443 eV). In this case, the position of the absorption peak exceeded the bandgap E_g NC perovskite. The absorption was caused by the appearance of an electron-hole pair in the NC perovskite. The photoluminescence was caused by the recombination of an electron-hole pair in the NC perovskite. The absorption and photoluminescence peaks were caused by interband transitions of an electron and were in the visible range of the spectrum. Synthesis of $CsPbI_3$ NCs achieved near-100 % PL quantum yield, highlighting their potential for efficient light harvesting [7].

In this work, unlike [49], we studied absorption caused by intraband electron transitions between the quantum-confined levels $E_{n,l+1}(a)$ and $E_{n,l}(a)$. In this case, the transition energies $\Delta E_{n,l}(a)$ (2) are in the IR region.

In [54], chemically stable solutions of NCs $CsPbI_3$ perovskite were synthesized using a new method. This method made it possible to introduce the organolead compounds trioctylphosphine-PbI_2 as a reactive precursor. As a result, the density of nonradiative recombination centers significantly decreased, and quenching PL in $CsPbI_3$ NCs was also greatly reduced. This made it possible to obtain a high quantum efficiency of photoluminescence at room temperature up to 100 % in perovskite NCs $CsPbI_3$. The effect of a high quantum efficiency of PL in NCs $CsPbI_3$ was due to the realization of the possibility of almost complete elimination of trapping defects.

Let us qualitatively estimate the appearance of nonlinear processes in nanosystems with NCs perovskites due to the photoionization of NCs perovskites. In a nanosystem with perovskite NC of radius *a*, when a quantum of light with energy

$$\hbar\omega_{n,l}(a) = E_{n,l}(a) \geq \Delta V \cong E_g, \qquad (18)$$

is absorbed, an electron from a quantum-confined level $E_{n,l}(a)$, located in NC enters the surrounding matrix of the NC. In the expression (18), ΔV is the ionization potential NC of the perovskite. ΔV has a value close to the bandgap E_g NC of the perovskite. Condition (18), taking into account (1), is satisfied for the quantum-confined states (*n*, *l*), which are described by the inequality

$$(X_{n,l})^2 \geq (2m_e\ a^2/\ \hbar^2)\ E_g. \qquad (19)$$

In nanosystems containing NCs perovskites $FAPbBr_3$ and $\{en\}FAPbBr_3$ with radii a = 5.5 nm, which were studied under experimental conditions [20], photoionization of NCs perovskites will occur, according to (18), only for highly excited quantum-confined electron levels (for example, for ($n \geq 7$, $l = 0$)). As the radius *a* decreases in NCs perovskites, the photoionization of electron quantum-confined states will also be observed for low-excited quantum-confined electron states (n, l). For

example, in NCs perovskites with radius $a = 1$ nm, there is only one quantum-confined electron level ($n=1$, $l=0$). At the same time, other low-excited quantum-confined electron states ($n \geq 1$, $l \geq 0$) arising in NCs perovskites will be photoionized. Thus, the theory of optical absorption on electron states of perovskites nanocrystals in weak optical fields that we have developed has an applicability criterion that is described by conditions (18) and (19).

In the nanosystems studied by us containing NCs perovskites $FAPbBr_3$ and {en}$FAPbBr_3$ with small radii a (if the conditions (18), (19) are met) the probability of trapping electrons in NCs perovskites should be low. Therefore, there will apparently be a significant quantum efficiency of PL in these NCs perovskites.

In the experimental work [54], the possessing PL blinking in $MAPbI_3$ perovskite submicrometer crystals. In such $MAPbI_3$ perovskite crystals of large sizes, quantum confinement and Auger recombination of electrons and holes were absent. It was found that PL blinking in $MAPbI_3$ perovskite submicrometer crystals was due to the reversible quenching of a single emitter which could possess non-Poisson statistics due to a local Auger process. In doing so, photoluminescence blinking in $MAPbI_3$ perovskite was called reversible switching between the active and passive state of the supertrap (an efficient recombination center). The perovskites NCs have a small finite number of quantum-confined levels of the electron and hole. Therefore, the emergence of multiphoton states with non-Poisson statistics due to the local Auger process is apparently unlikely in the perovskites NCs. Also unlikely is the creation of conditions for the observation of the possessing PL blinking in the perovskites NCs [58–64].

PROSPECTS OF SOLAR CELLS CONTAINING PEROVSKITE NANOSTRUCTURES

Solar cells, often referred to as photovoltaic (PV) cells, use the photovoltaic effect to convert light energy into electricity. They are considered one of the most environmentally friendly energy sources, along with hydropower and wind/tidal power. PV technologies have been consistently developed over the past few decades to improve the efficiency of these devices while keeping manufacturing costs low.

Solar cell technology is divided into three generations – see Fig. 1. (Si)-based technologies, including single crystals, multicrystalline Si, and hydrogenated amorphous (a-Si:H), belong to the first generation of solar cells. The second generation encompasses thin-film technologies. This category includes gallium arsenide (GaAs), cadmium telluride (CdTe), and copper indium selenide (CuInSe or CIGS) (and similar) based material systems. The third generation includes thin-film technologies of new materials, their potential properties surpass those of current technologies. This group of materials includes dye-sensitized solar cells (DSSC), perovskite and organic-based solar cells, and QDs photovoltaic cells [16–19].

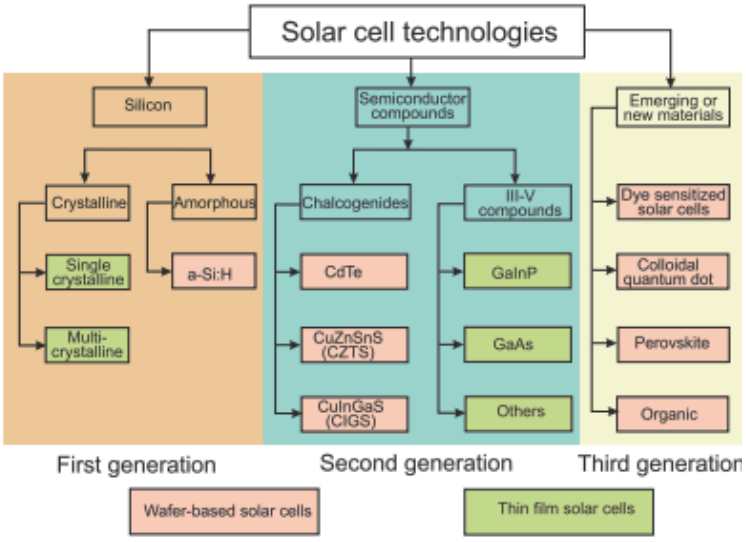

Fig. 1. Three generations of solar cells [16]

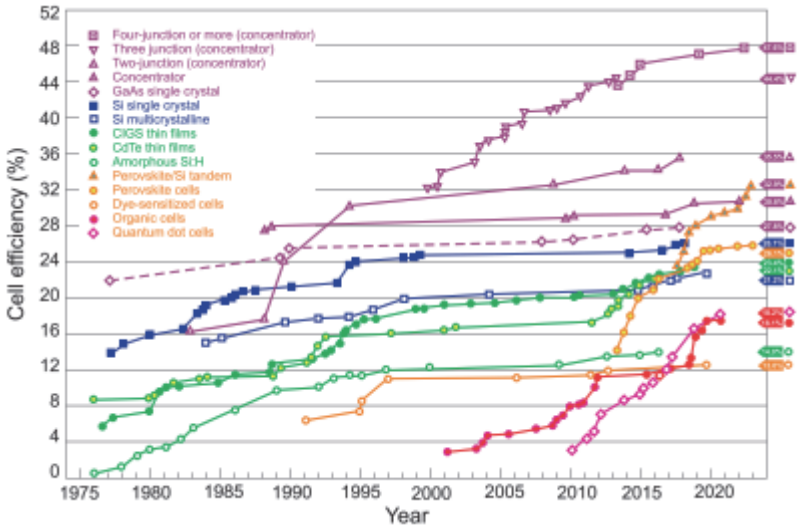

Fig. 2. The reported timeline of the solar cell energy power conversion efficiency (PCE). PCE records for perovskite cells are compared with the selected PV technologies, withcurrent records of ≈ 25.7 % for single junction perovskite devices [16]

Metal halide perovskite devices have become groundbreaking photovoltaic devices and have been implemented in many devices. They have been particularly recognized as the leader in PV technology due to the efficiency achieved over the last decade. Since the first reported device with a of efficiency ≈ 2.2 % in 2007, many improvements have been made to the perovskite structure, leading to a efficiency of ≈ 26.1 % (see Fig. 2) [16–18]. This rapid progress in the efficiency of converting light into electricity demonstrates the great potential of a new generation of inexpensive and newly efficient photovoltaic technology. It is expected that it will be possible to produce stable single-junction cells with efficiency of ≈ 28 % after proper improvement of interfacial materials and optimal device designs.

Perovskites have attracted extensive research interest due to their direct band gap, long carrier diffusion length, high absorption coefficients, and high defect tolerance. As a result, perovskites have demonstrated excellent performance in many devices with an understanding of solid-state physics, chemistry, and photophysics [16].

As shown in Fig. 3 *a* solar cell device consists of three main areas responsible for: photon absorption with subsequent carrier generation, carrier transport, and finally carrier extraction [19]. In the first region, dissociation of excitons generates electrons and holes. Since the binding energy of an electron-hole pair is much less than 300 K of thermal energy, the generation of free charge carriers occurs very quickly. Exciton dissociation occurs at the interface between the perovskite layer and the charge transport layer. Electrons are injected into the electron transport layer (ETL) and migrate to the anode (fluorine-doped tin oxide (FTO) – glass). At the same time, holes are injected into the hole transport layer (HTL) and then migrate to the metal cathode. As a result, the electrons/holes are collected by the electrodes to generate current in the external circuit. For organic materials, the upper and lower levels are the lowest unoccupied molecular orbital and the highest occupied molecular orbital, respectively [16–18].

Depending on the choice of the bottom element, three types of triple junction solar cells based on perovskite materials have been reported: 1) Perovskite /perovskite /perovskite (known as all-perovskite), 2) Perovskite /perovskite / Si, 3) Perovskite / perovskite /organic solar cells. The highest reported is efficiency of 23.3 % for all-perovskite, 22.2 % for perovskite /perovskite/Si, and 19.4 % for perovskite/perovskite/organic triple junction solar cells [19]. The optimal bandgap combination of triple junction solar cells depends on the properties of all layers and the different loss mechanisms and must be determined for each structure and the choice of interlayer materials. Another important criterion in series-connected multi-junction solar cells is current matching. In this type of solar cell, the

current cell is limited to the subcell that generates the least current. Therefore, to maximize the output current of the solar cell, the current generated in each cell must be the same.

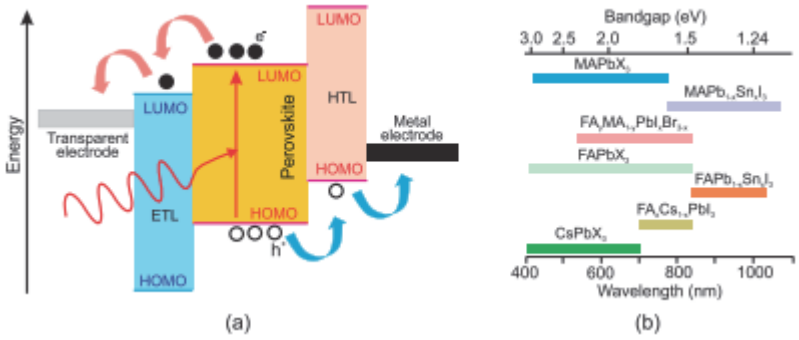

Fig. 3. PSCs: *a* – band diagram and operation principle (favorable energy band alignment affects the carriers' transport to the device's contacts), *b* – and bandgap values for perovskite materials [16]

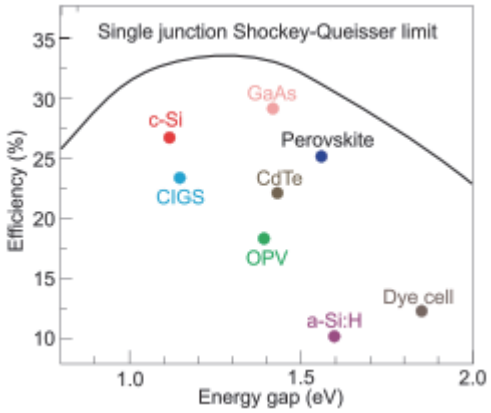

Fig. 4. Thermodynamic limit of the PCE for junction solar cells versus bandgap (Shockley-Queisser limit) compared to the utmost efficiencies for selected PV technologies [16]

To date, double-junction perovskite solar cells, especially those with lower Si elements, have already proven to be an attractive option for further improving the efficiency of future photovoltaic modules. Triple-junction perovskite solar cells can exceed the performance limit of double-junction solar cells and surpass the efficiency limit of double-junction solar cells. However, so far the focus has been on optimizing single and double solar cells and much less on developing ternary solar cells using perovskite semiconductors [10–18].

The efficiency of a junction solar cell is limited by the fundamental Shockley–Quisser limit (31–33 %). The maximum efficiency is achieved in the band gap range of 1.1–1.45 eV. As shown in Fig. 4, this includes technologically important photovoltaic semiconductors such as (see Fig. 2): crystalline Si (26.7 %), $Cu(In,Ga)Se_2$ (23.35 %), organic solar cell mixtures (18.2 %), GaAs (29.1 %), and CdTe (22.1 %). Other materials, such as a-Si : H (10.2 %) and most DSSCs, have slightly inflated bandgaps compared to the optimal region. Since lead halide perovskites can span a wider bandwidth, their highest efficiency has been estimated to be in the narrow range of 1.5–1.65 eV [16–19].

Analysis of the data in Figure 5 shows that the cost of solar energy has fallen significantly over the past few decades, and solar energy is very cheap. The cost of manufacturing Si panels has fallen, and the price of electricity from solar power plants is lower than that from fossil fuels. These trends further reinforce the importance of renewable energy from photovoltaic sources in the future [16–20].

Perovskite-based tandem solar cells have demonstrated efficiency improvements through

nanostructure integration and interface optimization, contributing significantly to PV progress [3].

Perovskite/Silicon tandem cells have advantages over other types of solar cells (Fig. 6). Thus, in [2] it is indicated that their efficiency reaches 30 %, which is 3–5 % higher than silicon cells. The advantage lies in their ability to absorb different ranges of light. In Perovskite/Silicon tandem cells [13] there is a technical possibility, unlike silicon cells, to change the composition of the perovskite to adjust the bandgap width, which opens up opportunities for optimizing performance in operation. The influence of molecular structure on the optical properties of azo-naphthalene dyes, which could inspire similar tuning in perovskites, is explored in [65], combining DFT and experimental approaches.

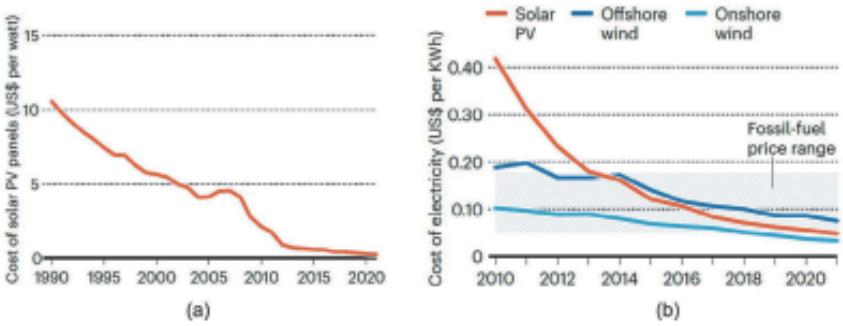

Fig. 5. The cost of producing: *a* – Si photovoltaic panels and *b* – electricity from selected sources. Reproduced with permission.[51] Copyright 2023, Springer Nature

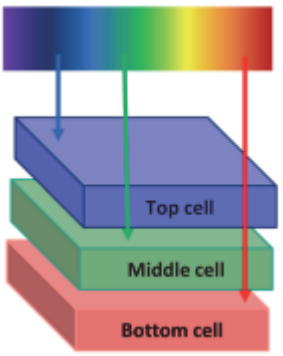

Fig. 6. Schematic diagram of the Perovskite/Silicon tandem cell for solar spectrum utilization by a triple junction solar cell consisting of a silicon bottom cell, a middle cell, and a top cell [7]

In addition to purely operational advantages, it is worth noting the economic aspect of this issue. Low-temperature processing of perovskite (below 150 °C) is economically more advantageous compared to high-temperature processes for GaAs or CIGS. The introduction of Perovskite/Silicon tandem elements into production does not require the restructuring of enterprises with silicon production lines [12].

CONCLUSIONS

Nanosystems containing NCs of $FAPbBr_3$ and {en}$FAPbBr_3$ exhibit exceptional optical properties in weak optical fields due to intraband electron transitions between quantum-confined states. Theoretical calculations revealed that at resonant IR frequencies, polarizabilities (e.g., $|A_2''| \approx 10^{-18}$ cm³) and absorption cross-sections ($\sigma_{abs} \approx 10^8$ cm²) achieve giant values, exceeding typical semiconductor values by two orders of magnitude. These results stem from enhanced dipole moments (e.g., D_{1,0,0}^{1,1,1} = 9.9 D₀ for {en}$FAPbBr_3$) and oscillator strengths (e.g., f_{1,0,0}^{1,1,1} = 0.33), confirming their potential as highly efficient, tunable IR absorbers for advanced nanophotonic applications [20–25, 49].

Currently, new PV technologies are striving to match the efficiency achieved by crystalline Si,

representing a technology close to commercialization. Compared to Si, PSCs have many advantages. Most importantly, unlike Si, perovskites exhibit a direct bandgap, allowing for much more efficient light absorption. As a result, only a thin film is required, reducing the cost of the fabrication process (low-cost solution processes). Unfortunately, a significant drawback has been sensitivity to moisture, air, and even light. Numerous research groups have experimented with different stabilization methods, but so far no PSC has demonstrated a durability close to that required for commercial solar cells (25 years) [12–16].

Rather than replacing Si, a better solution is expected to be the commercialization of perovskite/Si tandem cells. Since each material absorbs energy from different wavelengths of sunlight, perovskite/Si tandem cells have the potential to provide at least a 20 % higher energy efficiency than an Si cell. Tandem perovskite/Si photovoltaic cells have now achieved an efficiency exceeding 33 % efficiency in the laboratory, and their efficiency is much higher than that of Si and stand-alone cells [14–16].

Despite the excellent optoelectronic performance achieved by the new technology in both the normal contact and inverted *p-i-n* structures, there remain significant scientific challenges and industrial transformation bottlenecks that require urgent attention [10–19]: (1) The theoretical limit of PSCs with a bandgap of 1.53 eV is an efficiency of 31.34 % according to the Shockley–Queisser limiting theory. Although the efficiency of the most advanced new technology devices has reached an efficiency of 26.0 %, there is still a gap between this value and the limiting theory. Improving the efficiency of charge separation and transfer, as well as suppressing charge recombination are key challenges in current device research. (2) The key core of face-to-face interface design and energy band development is to find an effective physical model and clearly explain the carrier transport mechanism. (3) Research into new preparation methods and physical mechanisms will accelerate the practical application of new technologies.

Електронні стани нанокристалів перовскітів та майбутнє сонячних елементів (міні-огляд)

С.І. Покутній, Т.Ю. Громовий, В.М. Овденко

Інститут хімії поверхні ім. О.О. Чуйка Національної академії наук України
вул. Олега Мудрака, 17, Київ, 03164, Україна, pokutnyi.serg@gmail.com, grota@ukr.net
Інститут фізики Національної академії наук України
пр. Науки, 46, Київ, 03028, Україна
Кафедра хімії високомолекулярних сполук Київського національного університету імені Тараса Шевченка
вул. Володимирська, 60, Київ, 01033, Україна, valeryovdenko@gmail.com

Перовскітні матеріали, такі як формаміdиній бромід свинцю ($FAPbBr_3$) і легований етилендіамонієм $FAPbBr_3$ ($\{en\}FAPbBr_3$), широко використовуються в нанооптоелектронних пристроях завдяки відносно простому процесу виготовлення, низькій вартості та високій ефективності. Було досягнуто суттєвих результатів у теоретичних і експериментальних дослідженнях випромінювання та поглинання світла, продуктивності виявлення та конструкції пристроїв, особливо для роботи у видимій та ближній інфрачервоній (NIR) областях. Розглядаються можливості напівпровідникових перовскітних сонячних елементів (PSC) як надійного кандидата для збору сонячної енергії наступного покоління.

Теоретично показано, що в наносистемі, яка взаємодіє з випромінюванням низької інтенсивності, осциляторні сили переходів, а також дипольні моменти переходів для одночастинкових електронних квантово-вимірних станів, які виникають у перовскітах, що містять нанокристали (НК) $FAPbBr_3$ та $\{en\}FAPbBr_3$, набули значень, що на два порядки перевищували типові величини відповідних напівпровідників. Встановлено, що на резонансній частоті електронного переходу величини максимального оптичного поглинання НК, а також поляризовності НК набували гігантських значень, які перевищували на сім порядків ці величини на інших частотах. Це дає можливість використовувати такі наносистеми як наноматеріали, що сильно поглинають в широкому діапазоні інфрачервоних (ІЧ) хвиль з довжинами хвиль, які можна варіювати залежно від типу контактуючих матеріалів.

В даний час нові перовскітні технології спрямовані на досягнення ефективності перетворення сонячної енергії по відношенню до кристалічного кремнієвого (Si) елемента. У порівнянні з кремнієвого (Si) елемента, перовскітні сонячні елементи (PSC) мають багато переваг. На відміну від Si, перовскіти демонструють пряму заборонену зону, що дозволяє набагато ефективніше поглинати світло. У результаті потрібна лише тонка плівка, що знижує вартість виробничого процесу (недорогі процеси розчинення). На жаль, істотним недоліком є їхня чутливість до вологи, повітря і навіть світла. Численні дослідницькі групи експериментували з різними методами стабілізації, але поки що жоден PSC не продемонстрував довговічність, близьку до тієї, яка потрібна для комерційних сонячних елементів (25 років). Очікується, що замість заміни кремнію найкращим рішенням будуть тандемні елементи перовскіт/кремній. Оскільки кожен матеріал поглинає енергію сонячного світла з різною довжиною хвилі, тандемні елементи з перовскіту та кремнію можуть забезпечити принаймні на 20 % більшу енергоефективність, ніж кремнієвий елемент. Тандемні перовскітно-кремнієві фотоелектричні елементи тепер досягли ефективності понад 33 % у лабораторних умовах, і їхня ефективність набагато вища, ніж у кремнієвих та автономних елементів.

***Ключові слова**: Перовскітні нанокристали (НК), квантові точки (КТ), нанооптоелектронні пристрої, перовскітні сонячні елементи, квантово-вимірні стани електронів*

REFERENCES

1. Sen S., Gopalan S., Sellappan R., Grace, A.N., Sonar P. Tin-based eco-friendly perovskites for sustainable future. *Adv. Energy Sustainability Res.* 2023. **4**(12): 2300110.
2. Roy P., Ghosh A., Barclay F., Khare A., Cuce E. Perovskite solar cells: a review of the recent advances. *Coatings*. 2022. **12**(8): 1089.
3. Li C., Sun S., Gan D., Dou D., Li L. Perovskite single crystals: physical properties and optoelectronic. *Mater. Futures*. 2023. **2**(4): 042101.
4. Pham H.D., Yang T. C.-J., Jain S. M., Wilson G. J., Sonar P. Development of dopant-free organic hole transporting materials for perovskite solar cells. *Adv. Energy Mater*. 2020. **10**(13): 1903326.
5. Heydarian M., Heydarian M., Schygulla P.S., Reichmuth K., Bett A.J., Hohl-Ebinger J., Schindler F., Hermle M., Schubert M.C., Schulze P.S.C., Borchert J., Glunz S.W. Recent progress in monolithic two-terminal perovskite-based triple-junction solar cells. *Energy Environ. Sci*. 2024. **17**(5): 1781.
6. Park J., Kim J., Yun H.-S., Paik M.J., Noh E., Mun H.J., Kim M.G., Shin T.J., Seok S.I. Controlled growth of perovskite layers with volatile alkylammonium chlorides. *Nature*. 2023. **616**: 724.
7. Li N., Feng A., Guo X., Wu J., Xie S., Lin Q., Jiang X., Liu Y., Chen Z., Tao X. Engineering the hole extraction interface enables single-crystal $MAPbI_3$ perovskite solar cells with efficiency exceeding 22 % and superior indoor response. *Adv. Energy Mater*. 2022. **12**(7): 2103241.
8. Yang C., Yin J., Li H., Almasabi K., Gutiérrez-Arzaluz L., Gereige I., Brédas J.-L., Bakr O.M., Mohammed O.F. Engineering surface orientations for efficient and stable hybrid perovskite single-crystal solar cells. *ACS Energy Lett*. 2022. **7**(4): 1544.
9. Huang Z., Bai Y., Huang X., Li J., Wu Y., Chen Y., Li K., Niu X., Li N., Liu G., Zhang Y., Zai H., Chen Q., Lei T., Wang L., Zhou H. Anion–π interactions suppress phase impurities in $FAPbI_3$ solar cells. *Nature*. 2023. **623**: 531.
10. France R.M., Geisz J.F., Song T., Olavarria W., Young M., Kibbler A., Steiner M.A. Triple-junction solar cells with 39.5 % terrestrial and 34.2 % space efficiency enabled by thick quantum well superlattices. *Joule*. 2022. **6**(5): 1121.
11. Peplow M. A new kind of solar cell is coming: is it the future of green energy? *Nature*. 2023. **623**: 902.
12. Jiang P., Acharya D., Volonakis G., Zacharias M., Kepenekian M., Pedesseau L., Katan C., Even J. Pb-free halide perovskites for solar cells, light-emitting diodes, and photocatalysts. *APL Mater*. 2022. **10**: 060902.
13. Rogalski A. Progress in quantum dot infrared photodetectors. In: *Quantum Dot Photodetectors*. (Springer, Berlin, 2021).
14. Zhao Y., Yin X., Li P., Ren Z., Gu Z., Zhang Y., Song Y. Multifunctional perovskite photodetectors: from molecular-scale crystal structure design to micro/nano-scale morphology manipulation. *Nano-Micro Lett*. 2023. **15**: 187.
15. Li G., Wang Y., Huang L., Sun W. Research progress of high-sensitivity perovskite photodetectors: a review of photodetectors: noise, structure, and materials. *ACS Appl. Electron. Mater*. 2022. **4**: 1485.
16. Rogalski A., Wang F., Wang J., Martyniuk P., Hu W. The perovskite optoelectronic devices – a look at the future. *Small Methods*. 2025. **9**(1): 2400709.

17. Koh T.M., Fu K., Fang Y., Chen S., Sum T.C., Mathews N., Mhaisalkar S.G., Boix P.P., Baikie T. Formamidinium-containing metal-halide: An alternative material for near-IR absorption perovskite solar cells. *J. Phys. Chem. C.* 2013. **118**(30): 16458.
18. Kim J.Y., Lee J.-W., Jung H.S., Shin H., Park N.-G. High-efficiency perovskite solar cells. *Chem. Rev*. 2020. **120**(15): 7867.
19. Gray J.L. The physics of the solar cellin. In: *Handbook of Photovoltaic Science and Engineering*. (John Wiley & Sons, Ltd., 2011).
20. Pokutnyi S.I. Exciton spectroscopy with spatially separated electron and hole in Ge/Si heterostructure with germanium quantum dots. *Low Temperature Physics.* 2018. **44**(8): 819.
21. Pokutnii S.I. Absorption and scattering of light in quasi-zero-dimensional structures: II. Absorption and scattering of light by single-particle local states of the charge carriers. *Physics of the Solid State.* 1997. **39**(4): 528.
22. Efros A.L., Efros Al.L. Interband absorption of light in a semiconductor sphere. *Soviet physics – Semiconductors*. 1982. **16**(7): 772.
23. Pokutnii S.I. Absorption and scattering of light in quasi-zero-dimensional structures: I. Transition dipole moments of the charge carriers. *Physics of the Solid State.* 1997. **39**(4): 634.
24. Pokutnyi S.I., Kulchin Y.N., Dzuyba V.P. Binding energy of excitons formed from spatially separated electrons and holes in insulating quantum dots. *Semiconductors.* 2015. **49**(10): 1311.
25. Klyuev V.G., Volykhin D., Pokutnyi S.I., Ovchinnikov O.V. Relationship between structural and optical properties in colloidal CdxZn1-xS quantum dots in gelatin. *Journal of Nanophotonics.* 2016. **10**: 033507.
26. Ye Z., Cao T., O'Brien K., Zhu H., Yin X., Wang Y., Louie S.G., Zhang X. Probing excitonic dark states in single-layer tungsten disulphide. *Nature*. 2014. **513**: 214.
27. Ye Y., Wong Z.J., Lu X., Ni X., Zhu H., Chen X., Wang Y., Zhang X. Monolayer excitonic laser. *Nat. Photonics*. 2015. **9**(11): 733.
28. Blancon J.C., Tsai H., Nie W., Stoumpos C.C., Pedesseau L., Katan C., Kepenekian M., Soe C.M., Appavoo K., Sfeir M.Y., Tretiak S., Ajayan P.M., Kanatzidis M.G., Even J., Crochet J.J., Mohite A.D. Extremely efficient internal exciton dissociation through edge states in layered 2D perovskites. *Science.* 2017. **355**(6331): 1288.
29. Zhang Q., Chu L., Zhou F., Ji W., Eda G. Excitonic properties of chemically synthesized 2D organic-inorganic hybrid perovskite nnosheets. *Adv. Mater*. 2018. **30**(18): 1704055.
30. Baranowski M., Plochocka P. Excitons in metal-halide perovskites. *Adv. Energy Mater*. 2020. **10**(26): 1903659.
31. Nayak P.K., Mahesh S., Snaith H.J., Cahen D. Photovoltaic solar cell technologies: analysing the state of the art. *Nat. Rev. Mater*. 2019. **4**: 269.
32. Sutherland B.R., Sargent E.H. Perovskite photonic sources. *Nat. Photonics*. 2016. **10**: 295.
33. Palmstrom A.F., Eperon G.E., Leijtens T., Prasanna R., Habisreutinger S.N., Nemeth W., Gaulding E.A., Dunfield S.P., Reese M., Nanayakkara S., Moot T., Werner J., Liu J., To B., Christensen S.T., McGehee M.D., van Hest M., Luther J.M., Berry J.J., Moore D.T. Enabling flexible all-perovskite tandem solar cells. *Joule*. **3**(9): 2193.
34. Leijtens T., Bush K.A., Prasanna R., McGehee M.D. Opportunities and challenges for tandem solar cells using metal halide perovskite semiconductors. *Nat. Energy*. 2018. **3**: 828.
35. McMeekin D.P., Mahesh S., Noel N.K., Klug M.T., Lim J., Warby J.H., Ball J.M., Herz L.M., Johnston M.B., Snaith H.J. Solution-processed all-perovskite multi-junction solar cells. *Joule*. 2019. **3**(2): 387.
36. Tian X., Stranks S.D., You F. Life cycle energy use and environmental implications of high-performance perovskite tandem solar cells. *Sci. Adv*. 2020. **6**(31): 0055.
37. McCall K.M., Morad V., Benin B.M., Kovalenko M.V. Efficient lone-pair-driven luminescence: structure-property relationships in emissive metal halides. *ACS Mater. Lett*. 2020. **2**(9): 1218.
38. Lee S.W., Bae S., Kim D., Lee H.S. Historical analysis of high-efficiency, large-area solar cells: toward upscaling of perovskite solar cells. *Adv. Mater*. 2020. **32**(51): 2002202.
39. Wu R., Yang B., Zhang C., Huang Y., Cui Y., Liu P., Zhou C., Hao Y., Gao., Yang J. Prominent efficiency enhancement in perovskite solar cells employing silica-coated gold nanorods. *J. Phys. Chem. C.* 2016. **120**(13): 6996.
40. Kumar P., Singh S., Gupta B.K. Future prospects of luminescent nanomaterial based security inks: from synthesis to anti-counterfeiting applications. *Nanoscale*. 2016. **8**(30): 14297.
41. Liu Y., Han F., Li F., Zhao Y., Chen M., Xu Z., Zheng X., Hu H., Yao J., Guo T., Lin W., Zheng Y. Inkjet-printed unclonable quantum dot fluorescent anti-counterfeiting labels with artificial intelligence authentication. *Nat. Commun*. 2019. **10**: 2409.
42. Ma T., Li T., Zhou L., Ma X., Yin J., Jiang X. Dynamic wrinkling pattern exhibiting tunable fluorescence for anticounterfeiting applications. *Nat. Commun*. 2020. **11**(1): 1811.
43. Lu Y., Lu J., Zhao J., Cusido J., Raymo F.M., Yuan J., Yang S., Leif R.C., Huo Y., Piper J.A., Robinson J.P., Goldys E.M., Jin D. On-the-fly decoding luminescence lifetimes in the microsecond region for lanthanide-encoded suspension arrays. *Nat. Commun*. 2014. **5**: 3741.

44. Akkerman Q.A., Rainò G., Kovalenko M.V., Manna L. Genesis, challenges and opportunities for colloidal lead halide perovskite nanocrystals. *Nat. Mater*. 2018. **17**(5): 394.
45. Granchak V.M., Sakhno T.V., Kuchmiy S.Ya. Light-emitting materials – active components of luminescent solar concentrators (Review). *Theor. Exp. Chem*. 2014. **50**(1): 1.
46. Stroyuk A.L., Andryushina N.S., Kuchmiy S.Ya., Pokhodenko V.D. Photochemical processes involving graphene oxide (Review). *Theor. Exp. Chem.* 2015. **51**(1): 1.
47. Jacak W.A. *Quantum nano-plasmonics*. (Cambridge University Press, 2020).
48. Laska M., Krzemińska Z., Kluczyk-Korch K., Schaadt D., Popko E., Jacak W.A., Jacak J.E. Metallization of solar cells, exciton channel of plasmon photovoltaic effect in perovskite cells. *Nano Energy*. 2020. **75**: 104751.
49. Jacak W.A., Jacak J.E. New channel of plasmon photovoltaic effect in metalized perovskite solar cells. *J. Phys. Chem. C.* 2019. **123**(50): 30633.
50. Kozitsky A.V., Stroyuk A.L., Raevskaya A.E., Kuchmiy S.Ya. Photoelectrochemical solar cells based on semiconductor nanoparticles and liquid electrolytes (Review). *Theor. Exp. Chem.* 2017. **53**(3): 135.
51. Pokutnyi S.I., Kulchin Y.N., Dzyuba V.P., Amosov A.V. Biexciton in nanoheterostructures of dielectric quantum dots. *J. Nanophotonics*. 2016. **10**(3): 036008.
52. Landau L.D., Lifshitz E.M. *Course of Theoretical Physics, Electrodynamics of Continuous Media*. Band 1. (Pergamon Press, New York, 1984).
53. Davydov A.S. *Quantum Mechanics*. (Elsevier, 1965).
54. De Roo J., Ibáñez M., Geiregat P., Nedelcu G., Walravens W., Maes J., Martins J.C., Van Driessche I., Kovalenko M.V., Hens Z. Highly dynamic ligand binding and light absorption coefficient of cesium lead bromide perovskite nanocrystals. *ACS Nano*. 2016. **10**(2): 2071.
55. Liu F., Zhang Y., Ding C., Kobayashi S., Izuishi T., Nakazawa N., Toyoda T., Ohta T., Hayase S., Minemoto T., Yoshino K., Dai S., Shen Q. Highly luminescent phase-stable CsPbI3 perovskite quantum dots achieving near 100 % absolute photoluminescence quantum yield. *ACS Nano*. 2017. **11**(10): 10373.
56. Suchikova Y., Kovachov S., Zhydachevskyy Y., Bohdanov I., Karipbayev Z.T., Popov A.I. Advanced synthesis and characterization of CdO/CdS/ZnO heterostructures for solar energy applications. *Materials*. 2024. **17**(7): 1566.
57. Suchikova Y., Kovachov S., Bogdanov I., Karipbaev Z.V., Pankratov V., Popov AI. Study of the structural and morphological characteristics of the $Cd_xTe_yO_z$ nanocomposite obtained on the surface of the CdS/ZnO heterostructure by the SILAR method. *Appl. Phys. A*. 2023. **129**: 499.
58. Suchikova Y.O., Bogdanov I.T., Kovachov S.S., Kamensky D.V., Myroshnychenko V.O., Panova N.Y. Optimal ranges determination of morphological parameters of nanopatterned semiconductors quality for solar cells. *Arch. Mater. Sci. Eng.* 2020. **101**(1): 15.
59. Balakhayeva R., Akilbekov A., Baimukhanov Z., Popov AI. Structure properties of CdTe nanocrystals created in SiO_2/Si ion track templates. *Surf. Coat. Technol*. 2020. **401**: 126269.
60. Balakhayeva R., Akilbekov A., Baimukhanov Z., Usseinov A., Giniyatova S., Zdorovets M., Vlasukova L., Popov A.I., Dauletbekova A. CdTe nanocrystal synthesis in SiO_2/Si ion-track template: the study of electronic and structural properties. *Phys. Status Solidi A. Appl. Mater. Sci.* 2021. **218**(1): 2000231.
61. Monge M.A., Popov A.I., Ballesteros C., Gonzalez R., Chen Y., Kotomin E.A. Formation of anion-vacancy clusters and nanocavities in thermochemically reduced MgO single crystals. *Phys. Rev. B.* 2000. **62**: 9299.
62. Popov A.I., Monge M.A., Gonzalez R., Chen Y., Kotomin E.A. Dynamics of F-center annihilation in thermochemically reduced MgO single crystals. *Solid State Commun*. 2001. **118**(3): 163.
63. Kotomin E.A., Kuzovkov V.N., Popov A.I. The kinetics of defect aggregation and metal colloid formation in ionic solids under irradiation. *Radiat. Eff. Defects Solids*. 2023. **155**(1–4): 113.
64. Bellucci S., Bolesta I., Cestelli G.M., Karbovnyk I., Lesivciv V., Micciulla F., Pastore R., Popov A.I. Cadmium clusters in CdI_2 layered crystals: the influence on the optical properties. *J. Phys.: Condens. Matter*. 2007. **19**(39): 395015.
65. Ovdenko V., Labunets A., Ronkovych A., Volochniuk M. Effect of nitrogen atom position in Sudan I-like azo-naphthalene dyes on linear and nonlinear optical properties: DFT and experimental study. *J. Mol. Struct.* 2025. **1333**: 14173.

Received 23.12.2024, accepted 04.09.2025